

Soft Matter

Accepted Manuscript



This is an *Accepted Manuscript*, which has been through the Royal Society of Chemistry peer review process and has been accepted for publication.

Accepted Manuscripts are published online shortly after acceptance, before technical editing, formatting and proof reading. Using this free service, authors can make their results available to the community, in citable form, before we publish the edited article. We will replace this *Accepted Manuscript* with the edited and formatted *Advance Article* as soon as it is available.

You can find more information about *Accepted Manuscripts* in the [Information for Authors](#).

Please note that technical editing may introduce minor changes to the text and/or graphics, which may alter content. The journal's standard [Terms & Conditions](#) and the [Ethical guidelines](#) still apply. In no event shall the Royal Society of Chemistry be held responsible for any errors or omissions in this *Accepted Manuscript* or any consequences arising from the use of any information it contains.

Turning up the heat on wormlike micelles with a hydrotopic salt in microfluidics

Joshua J. Cardiel,^{a,b} Ya Zhao,^a Pablo De La Iglesia,^c Lilo D. Pozzo,^c and Amy Q. Shen^{a,b,†}

Received Xth XXXXXXXXXXXX 20XX, Accepted Xth XXXXXXXXXXXX 20XX

First published on the web Xth XXXXXXXXXXXX 200X

DOI: 10.1039/b000000x

In equilibrium, wormlike micelles can transition from entangled to branched structures with increasing surfactant concentrations and ionic strength. Under flow conditions, structural transition of micellar solutions can follow very different trajectories. In this study we consider the flow of a semi-dilute wormlike micellar solution through an array of microposts, with focus on its rheological and microstructural evolutions. Specifically, the micellar solution (precursor) contains cationic surfactant cetyltrimethylammonium bromide (CTAB) and hydrotopic organic salt 3-hydroxynaphthalene-2-carboxylate (SHNC). We report the formation of a flow induced structured phase (FISP), with entangled, branched, and multi-connected micellar bundles, evidenced by electron microscopy and small-angle neutron scattering (SANS). By integrating gold-etched microheaters with the micropost design in a microfluidic device, we investigate the localized temperature effect on both the precursor and FISP, with complementary investigations from SANS. We observe that the FISP does not completely disintegrate at high temperatures, whereas, the precursor exhibits shortening of wormlike micelles as temperature increases. We also correlate the microstructure of both FISP and precursor with two point passive microrheology and bulk rheology characterizations.

1 Introduction

Surfactant molecules spontaneously self assemble in aqueous solutions above a critical micellar concentration (CMC). Mixing inorganic salts (e.g., sodium chloride, NaCl) or organic salts (e.g., 3-hydroxynaphthalene-2-carboxylate, SHNC) with cationic surfactants reduces electrostatic interactions within surfactant head groups and induces micellar growth^{1–6}. Structurally similar to surfactants, hydrotopic salts can act as strong “binding” additives and reduce surface tension in an aqueous solution. A number of organic hydrotopic salts such as NaSal⁷ and SHNC^{8,9} have been studied in combination with cationic surfactants because these mixtures can reduce the charge density of surfactant micellar aggregates significantly, enhancing ion pairing and surface activity of the micelles above a minimum hydrotopic concentration, and promoting growth of wormlike micelles at a much lower salt/surfactant ratio in comparison to other salts^{10–13}. In particular, hydrotopic organic salt SHNC has drawn considerable attention as HNC[–] ions (3-hydroxynaphthalene-2-carboxylic acid (HNC)) have exhibited sensitive responses under varying temperature, ionic strength, and flow conditions, due to

the strong hydrophobicity and naphthalene structure (two fused benzene rings) present in the SHNC (see Fig. 1). SHNC is thus considered as an anionic surfactant similar to SDS but with a shorter hydrophobic tail^{14–16}. Since a closer proximity and better interactions between carboxyl (position 2) and hydroxyl (position 3) groups are present in SHNC molecules, stronger bonds can be formed in wormlike micelles (see Fig. 1). Therefore, it is proposed that the specific geometry in SHNC is responsible for certain phase transition behavior in SHNC-cationic surfactant solutions when compared with other organic salts (e.g., NaSal)^{5,17,18}. For example, Mishra *et al.*^{19,20} investigated the phase behavior of an aqueous mixture of SHNC/CTAB by fixing the CTAB concentration at 60 mM and increasing the SHNC/CTAB molar ratio. They observed the transition of small micellar aggregates to a positively charged gel phase. Further increase of the SHNC induced the formation of a liquid crystallization lamellar phase, followed by a precipitate multi-lamellar vesicle phase at equal molar SHNC/CTAB concentration. They argued that the excess Na⁺ (from SHNC) and Br[–] (from CTAB) ions in the solution screened the electro-repulsive forces between vesicles and collapsed them into sticky and thick precipitates¹⁵. Moreover, micelles in cationic-SHNC solutions are very sensitive to temperature variations. Kalur *et al.*²¹ observed an unusual increase of the shear viscosity and relaxation time of a mixture of 280 mM SHNC and 60 mM of erucyl bis(hydroxyethyl)methylammonium chloride (EHAC) at elevating temperatures. Verma *et al.*²² reported the for-

† Electronic Supplementary Information (ESI) available: [details of any supplementary information available should be included here]. See DOI: 10.1039/b000000x/

^a Mechanical Engineering, University of Washington, Seattle, WA, USA

^b Micro/Bio/Nanofluidics Unit, Okinawa Institute of Science and Technology, Okinawa, Japan. E-mail: amy.shen@oist.jp

^c Chemical Engineering, University of Washington, Seattle, WA, USA

mation of elongated micelles and vesicles from SHNC/CTAB mixtures with excessive amount of SHNC, by using bulk rheometry and light scattering techniques. They proposed that HNC^- ions could desorb from the micelles and decrease the surface charge of micelles with elevating temperatures or dilution, promoting growth of wormlike micelles with enhanced viscoelasticity.

Recently, we reported the formation of a flow-induced structured phase (FISP) by using low concentrations of hydrotropic organic salt sodium salicylate ($[\text{NaSal}] = 16 \text{ mM}$ and $[\text{CTAB}] = 50 \text{ mM}$, with salt to surfactant molar ratio of 0.32)²³. We suggested that the formation of NaSal-based FISP was induced by spatial confinement, accompanied by local micellar concentration fluctuations and entropic fluctuations during the flow^{24–26}. Since SHNC has dual benzene rings in comparison to the single benzene ring structure in NaSal, stronger hydrophobicity and noncovalent interactions between adjacent micelles are expected as hydrophobic HNC^- ions need to be shielded from water to stabilize these micelles. Consequently, domains of $\pi-\pi$ ions are paired and cation- π groups are formed between HNC^- ions and adjacent hydrophobic CTAB headgroups, inducing stable and more extensible micellar networks that exhibit versatile response under temperature variations²¹. Further, the high hydrophobicity of SHNC induces denser micellar structural formation that could be used as micro-membranes for flow separations^{19,21,27,28} and encapsulation of nano/micro entities^{29,30}. Motivated by the formation of NaSal-based FISP and the temperature sensitive nature of SHNC, we explored the formation of SHNC-based FISP with thermal effects in this work. In particular, we focused on the aqueous mixture of SHNC/CTAB ($[\text{SHNC}] = 14.4 \text{ mM}$ and $[\text{CTAB}] = 45 \text{ mM}$, with salt to surfactant molar ratio of 0.32). We used a microfluidic device consisting of hexagonal micro-post arrays (same device as used in Cardiel *et al.*²³) to form the FISP (see Fig. 1 and Fig. 3). The strong binding affinity (cation- π and $\pi-\pi$) between hydrophobic naphthalene structures in SHNC micelles greatly facilitates the formation of nanoporous FISP with strong viscoelastic properties under spatial confinement in microfluidics. We performed bulk rheological characterization of the original liquid precursor, as well as two point passive microrheology of the FISP. We used small-angle neutron scattering (SANS), transmission electron microscopy (TEM), and scanning electron microscopy (SEM) to characterize the microstructure of the FISP.

2 Materials and Methods

2.1 Precursor preparation

The wormlike micellar solution (precursor) was an aqueous mixture of the cationic surfactant cetyltrimethylammonium bromide (CTAB), purchased from Sigma-Aldrich (Saint Louis,

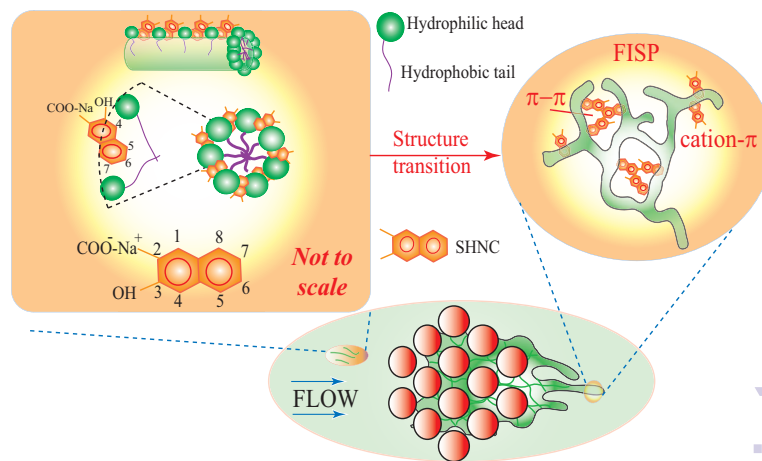


Fig. 1 The naphthalene structure present in SHNC favors curvature change and ion pairing of CTAB micelles and induces uni-dimensional growth of wormlike micelles (precursor). The 4, 5, 6, and 7 positions are present in a nonpolar environment inside the micelles¹⁹. When the precursor is subjected to high strain rates of $\sim 3.7 \times 10^4 \text{ s}^{-1}$ and total strain of $\sim 2.1 \times 10^3 \text{ s}^{-1}$, entangled micellar networks (FISP) begin to emerge.

MO), and hydrotropic organic salt 3-hydroxy naphthalene-2-carboxylate (SHNC), purchased from TCI America (Portland, OR). All chemicals were used as received. The solution was prepared by adding the appropriate amount of CTAB and SHNC to deionized (DI) water and mixed for 24 hours. The precursor was left at rest for 1 week to equilibrate. The precursor concentration was fixed at $[\text{CTAB}] = 45 \text{ mM}$ with the molar ratio $R = [\text{SHNC}]/[\text{CTAB}] = 0.32$, which falls under semi-dilute regime (see details in supporting information).

2.2 Microfluidic Device Fabrication

The microfluidic devices were fabricated by using standard soft lithography techniques.³¹ Briefly, a thin layer of SU-8 2050 photoresist (MicroChem Corp., Newton, MA) was spun onto a silicon wafer and cured. A Heidelberg $\mu\text{PG}-101$ machine (Heidelberg Instruments GmbH, Heidelberg, 45 Germany) at $4\times$ speed and 75% of 18 mW was applied to write the mold of microchannel onto the photoresist. The wafer was subsequently cured, developed, and surface treated to render it hydrophobic. Modeling glue sticks the silicone tubing ports at the designated inlets and outlets of the microchannel. A 10:1 mixture of Sylgard 184-PDMS elastomer was poured onto the etched wafer, desiccated, and cured at 60°C for ~ 1 hour. The resulting PDMS cast was peeled off from the wafer and plasma bonded onto a glass slide using a Femto plasma cleaner (Diener Electronic). A syringe pump (Harvard apparatus) was used to pump the precursor solution into the device through the inserted polyethylene tubing (Intramedic). The PDMS-

glass microfluidic device has a channel height of $\sim 75 \mu\text{m}$ and total channel width of 1.26 mm containing hexagonal arrays of microposts with diameter of $100 \mu\text{m}$ and spacing of $15 \mu\text{m}$.

2.3 Microheater Device Fabrication

Gold etched microheaters were fabricated to study the localized temperature behavior of the FISP and the precursor. We used gold liftoff procedure to pattern the microheaters onto glass cover slides (GCS). First, a layer of chrome ($\sim 15 \text{ nm}$) was deposited onto a GCS by using chemical vapor deposition process (CVD). Next, a second layer of gold ($\sim 200 \text{ nm}$) was deposited on the GCS with the chrome layer by using CVD process. Finally, the photoresist (AZ-1512) was spun onto the gold-chrome-GCS at 3000 RPM, a nominal thickness of $\sim 1.2 \mu\text{m}$ was obtained. The AZ-1512 photoresist coated gold-chrome-GCS was then exposed with the microheater design and subsequently developed. The remaining AZ-1512 photoresist and the metal on top of the GCS, were removed by using chrome etching and gold etching processes and an acetone bath. Fig. 2A shows the final gold etched microheater patterned onto the GCS. After the microheaters were fabricated, we bonded them onto the PDMS microchannel containing the hexagonal microposts array. Fig. 2B illustrates the microheater location with respect to the micropost array, showing FISP fingers formed at room temperature. DC voltage and current was applied to vary the resistance of the microheater as a mean to vary the temperature. The microheater and a thermocouple were connected to a power source and computer with a LabView program to control the temperature. The experimental error of the microheater was $\sim 1.5 \pm 0.3 \text{ }^\circ\text{C}$ based on the calibration.

2.4 Bulk Shear Rheometry

The viscoelastic properties of the precursor solution were characterized by using a stress controlled rheometer (AR2000, TA Instruments). All measurements were performed by using an aluminum cone and plate geometry (60 mm diameter and angle 1°) with a truncation gap of $59 \mu\text{m}$. The temperature was maintained at $25 \text{ }^\circ\text{C}$ and a solvent trap was used to prevent evaporation.

2.5 Microrheology

Due to small volumes of the FISP produced in the microdevice ($\sim 100 \mu\text{L}$), rheological properties of the FISP were measured by two point passive microrheology³². Two point passive microrheology (2PPM) relates the thermal motion of tracer particles embedded in a sample to approximate its rheological properties. 2PPM does not depend on the shape and size of the tracer particle. Most importantly, it is independent of the coupling between the medium and tracer particles. 2PPM correlates the strain field of one tracer particle

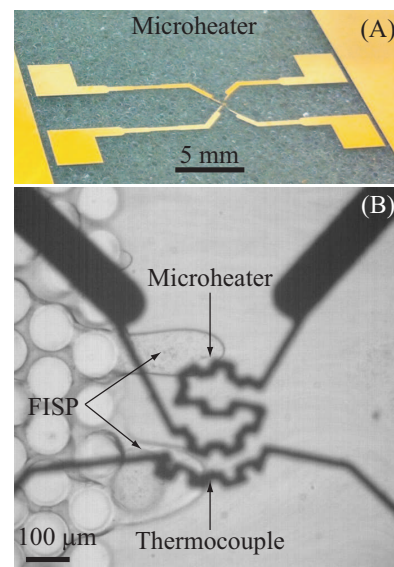


Fig. 2 (A) Gold etched microheater used to study the temperature response of the FISP. (B) Microheater (GCS) bonded onto the PDMS substrate containing the hexagonal microposts array. (B) Finger like FISP formed at room temperature.

to a second tracer particle³². Hence 2PPM is a good approximation to measure rheological properties of highly inhomogeneous materials^{32–34}. From the TEM and SEM images, FISP exhibited highly inhomogeneous microstructures with large range of pore size. Employing 2PPM provides a good estimate to the FISP's rheology. To facilitate these measurements, the precursor solution was seeded with $1 \mu\text{m}$ diameter polystyrene tracer particles, with $\sim 0.3 \text{ wt}\%$ in the total solution. The experiments were conducted on an inverted Leica microscope at $23 \pm 1.5 \text{ }^\circ\text{C}$. In addition, the heat generated by the microscope lamp slightly increases the temperature in the microchannel. Hence, the local temperature in the microchannel during the microrheology experiments is $\sim 25 \text{ }^\circ\text{C}$. After a sufficient amount of FISP was produced in the microchannel, we waited for ~ 2 hours before conducting the 2PPM measurements. An area of the FISP containing more than 200 tracer particles per video was imaged at a magnification of $150\times$ (PL Fluotar 100×1.30 oil objective with a $1.5\times$ tube lens), and videos consisting of 2048 frames were taken at 60 fps with a high-speed camera (Photron FASTCAM). To avoid wall effects, the focal plane was set at $\sim 30 \mu\text{m}$ from the bottom and top parts of the microchannel. A total of 25 videos were analyzed to approximate the averaged rheological properties of the FISP.

From the cross-correlated thermal motion of particle pairs, we determined the complex modulus $G^*(\omega)$ of both precursor and FISP^{32–34}. The complex modulus comes from the Stokes–Einstein relation, which shows that the shear stress

relaxation in the locality of the particle is identical to that of the bulk fluid subjected to a shear strain³⁵. The complex modulus is defined as $G^*(\omega) = G'(\omega) + iG''(\omega)$, where ω is the frequency, $G'(\omega)$ is the elastic modulus, and $G''(\omega)$ is the viscous modulus. We used multiparticle tracking video-microscopy to measure the two-dimensional mean-square displacement ($\text{MSD} = \langle \Delta r^2(t) \rangle$) of the embedded microbeads in the FISP³⁶. We then calculated the pairwise cross-correlated bead displacements as a function of separation distance r and lag time τ , and the component in the direction of bead separation, $D_{rr}(r, \tau)$ was used to extract $G^*(\omega)$ ^{32–35}. The correlated motion (in Laplace space) of two tracer particles can be defined as³²:

$$\tilde{D}_{rr}(r, s) = \frac{k_B T}{2\pi r s \tilde{G}(s)}, \quad (1)$$

where the MSD is related to D_{rr} through

$$\langle \Delta r^2(\tau) \rangle_D = 2 \frac{r}{a} D_{rr}(r, \tau), \quad (2)$$

and the complex modulus ($G^*(\omega)$) can be obtained by Fourier transform $\tilde{G}(s)$ such as^{35,37}:

$$\tilde{G}(s) = |G^*(\omega)| \approx \frac{k_B T}{\pi a \langle \Delta r^2(\frac{1}{\omega}) \rangle \Gamma(1 + \alpha(\omega))}, \quad (3)$$

where k_B is the Boltzmann constant, T is the absolute temperature, a is the radius of the tracer particle, Γ is the gamma function, and

$$\alpha(\omega) = \frac{d(\ln(\Delta r^2(\omega^{-1}))}{d(\ln(\omega^{-1}))} \quad (4)$$

is the logarithmic slope of the MSD. From the complex modulus the viscoelastic response ($G'(\omega)$ and $G''(\omega)$) of the FISP can be approximated. Since 2PPM approximates $\langle \Delta r^2(\tau) \rangle$ locally by a second order polynomial in the logarithmic scale to extract $G^*(\omega)$ ³², it neither requires the experimental data to be fit to an analytical model, nor does it suffer from truncation errors of numerical integrations.

2.6 Neutron Scattering Measurements

SANS and ultra small angle neutron scattering (USANS) measurements were performed on the same samples at the National Institute of Standards and Technology (NIST) Center for Neutron Research (NCNR) in Gaithersburg, Maryland. SANS was performed using a standard configuration to cover a wide range of wave vector values. USANS measurements were performed by using a perfect crystal diffractometer BT5 at the NCNR³⁸. USANS increases the scattering range, so that sub-micron and micron sized features of the FISP could also be probed. The samples were tested at four temperatures: 25 °C, 30 °C, 45 °C, and 60 °C. Analysis and model

fitting was performed using the DANSE SansView software³⁹. Note that only smeared data was fitted, and the models were modified to account for the line-collimation of the system using the tools available in the software package. The precursor was prepared by volume in deuterated water containing 99.9% D₂O (Cambridge Isotope Laboratories, Andover, MA). Since the conversion rate from the precursor to the FISP scaffold is not 100% from the microfluidic process, we collected the sample from the microchannel containing the FISP scaffold and liquid precursor residues. We then added 15 mL of D₂O and centrifuged the diluted solution at 1500 RPM for 30 minutes. We left the centrifuged solution without agitation for 5 hours before experiments. A supernatant thin layer containing the concentrated FISP structure was formed in the stored solution at room temperature (see support information). We then loaded ~100 μL of the FISP suspended in D₂O in a demountable, 2 mm titanium cell with quartz windows (NIST). The demountable cell was filled with the dispersion and capped with a screw. The cell was gently shaken to obtain homogenous dispersion before samples were exposed to the neutron beam in the SANS instrument. Subsequently the samples were again agitated before in the cell before the USANS measurement. The scattering contrast was determined from the scattering length density (SLD) of the deuterated solvent ($6.39 \times 10^{-6} \text{ \AA}^{-2}$) and the precursor ($-1.54 \times 10^{-7} \text{ \AA}^{-2}$) by using SANSview tool bar³⁹.

2.7 Electron Microscopy

After a sufficient amount of FISP was formed for SEM and TEM studies, the microchannel was rinsed with DI water to remove any residue precursor that did not convert to FISP. We then waited for 3 hours before preparing the TEM and SEM samples. TEM grids (Cu-100 mesh; Electron Microscopy Sciences) were placed on a freshly opened holder covered with the FISP. After 30 s, a 5 μL drop of NanoW negative stain (Nanoprobes, Inc) was applied on the material to enhance imaging contrast. After another 30 s, the residual liquid was blotted off with filter paper and left to air-dry. The same sample preparation procedure was adopted for SEM.

TEM samples were imaged by the Tecnai G2 F20 transmission electron microscope (FEI Co., Hillsboro, OR) at 200 kV and equipped with a field emission gun. Images were recorded under low dose conditions at a magnification of 50,000 and a pixel spacing of 2.2 \AA on a 4k CCD camera (4k Eagle Camera, FEI). SEM samples were imaged with a FEI helios scanning electron microscope at 3–5 kV. After we imaged the FISP structure in the TEM, we used the same grids for SEM imaging. We performed Au-sputter on the TEM grids containing the FISP structure. The sputtering lasted for 30 seconds on a SPI Module Sputter/Carbon Coater. After the grids coated with FISP structures were sputtered, we loaded the grids in the

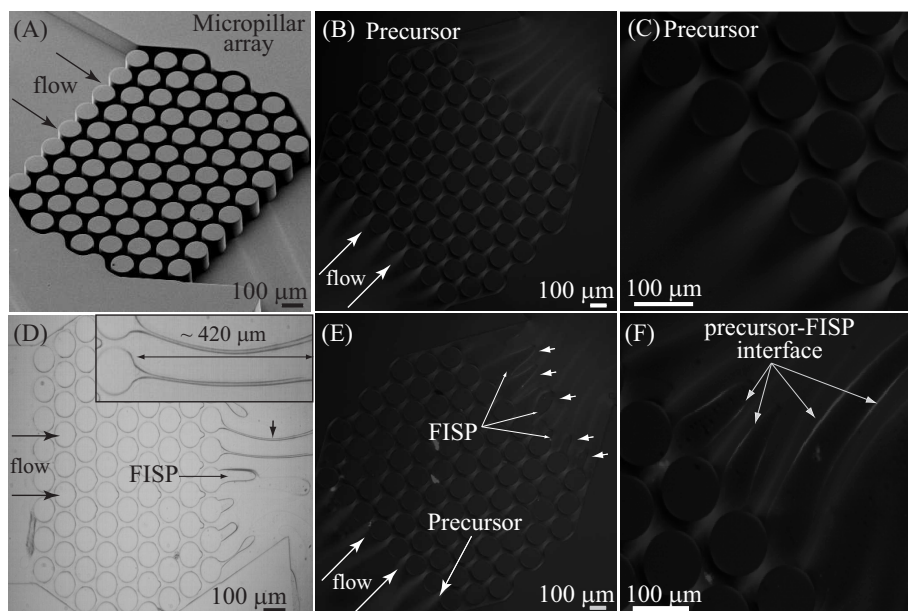


Fig. 3 (A) SEM image of the hexagonal micropost array to produce FISP. (B&C) Flow birefringence of the precursor. Bright bands indicate the existence of anisotropic micellar structures. (D) Snapshot of the FISP formation showing FISP-like fingers under bright-field microscopy. The inset shows the formation of long FISP filaments, illustrating viscoelastic nature of the FISP. Left arrows represent the flow direction. While the middle arrow represent the area where FISP was formed. (E) The interior of FISP does not exhibit birefringence, the small-white arrows highlight flow birefringence at the precursor-FISP interface. (F) Precursor-FISP interface exhibits birefringence response. The experiments were performed at $\sim 25^\circ\text{C}$.

scanning electron microscope for imaging.

3 Results and Discussions

3.1 Formation of FISP

By using similar devices reported by Cardiel *et al.*²³, we suggested that the same mechanism to form NaSal based FISP can be used to form SHNC based FISP. The high stretching in the micropost array ($O(10^4 \text{ s}^{-1})$), entropic fluctuations and flow alignment enables SHNC ions to penetrate to the core of wormlike micelles at high frequency, increase flexibility of wormlike micelles, therefore reduce the curvature of the cylindrical part of the micelle^{24–26,40,41}. As a result, the free energy of surfactant molecules in the end-cap relative to the curvature energy in the cylindrical body of the micelle becomes larger, the energy required to interconnect wormlike micelles will decrease^{5,42–44}. Thus it becomes energetically favorable for flexible adjacent micelles to merge when they flow through the confined microposts, promoting the formation of FISP (see Fig. 3)^{26,42,45,46}. Fig. 3C exhibits the formation of FISP-like fingers; the inset in Fig. 3C qualitatively gives a sense of the high viscoelastic properties of the FISP, showing long sheet-like filaments ($\sim 420 \mu\text{m}$ of length, $\sim 75 \mu\text{m}$ of height and $\sim 5 \mu\text{m}$ in width) before rupture, indicating the high stretcha-

bility of the FISP structure.

An estimate of the strain rate and total strain was obtained by considering the rate of strain experienced by a fluid element as it enters the micropost array⁴⁷. The empty channel velocity is $\phi \hat{U}_{\text{avg}}$, and as the fluid element enters the array its velocity must increase to $\phi \hat{U}_{\text{avg}} (\hat{D} + \hat{d}) / \hat{d}$ over a distance of roughly \hat{D} , where \hat{d} is the spacing between the microposts. Thus the extensional strain resulting from this acceleration is

$$\hat{\gamma}_{\text{ext}} \approx \frac{1}{\hat{D}} \left(\phi \hat{U}_{\text{avg}} \frac{\hat{D} + \hat{d}}{\hat{d}} - \phi \hat{U}_{\text{avg}} \right) = \frac{\phi \hat{U}_{\text{avg}}}{\hat{d}} = \frac{\hat{Q}}{\hat{d} \hat{W} \hat{H}}. \quad (5)$$

If we approximate the flow through the gaps between the microposts as a 2D Poiseuille flow, the maximum velocity between two posts is $3\phi \hat{U}_{\text{avg}} (\hat{D} + \hat{d}) / (2\hat{d})$. Thus an estimate of the strain due to shear is

$$\hat{\gamma}_{\text{sh}} \approx \frac{3\phi \hat{U}_{\text{avg}}}{2\hat{d}} \frac{\hat{D} + \hat{d}}{\hat{d}} = \frac{3\hat{Q}}{2\hat{d} \hat{W} \hat{H}} \frac{\hat{D} + \hat{d}}{\hat{d}}, \quad (6)$$

adding the above two expressions we have

$$\hat{\gamma}_{\text{total}} \approx \frac{\hat{Q}}{\hat{d} \hat{W} \hat{H}} \left(\frac{5}{2} + \frac{3\hat{D}}{2\hat{d}} \right). \quad (7)$$

For a hexagonal array with posts of diameter $100 \mu\text{m}$ and a spacing of $15 \mu\text{m}$, $\phi = 0.31$ (see Fig. 3A). Then for a flow rate

of 15 mL/h and the channel dimensions given in the materials and methods section, equation (7) gives $\dot{\gamma}_{\text{total}} \approx 3.7 \times 10^4 \text{ s}^{-1}$. The average velocity can be calculated as $\dot{U}_{\text{avg}} \approx 0.21 \text{ m/s}$, while the average residence time of a fluid element is $\dot{L}/\dot{U}_{\text{avg}} \approx 0.057 \text{ s}$. Hence the total strain was estimated as $\dot{\gamma} \approx 2100$.

There have been reports that SHNC based wormlike micelles exhibit flow birefringence at high salt concentrations ($>80 \text{ mM}$)^{19,20,48}. Frounferker *et al.*⁴⁸ reported persistent birefringence in samples containing 40 mM EHAC and 80–240 mM of sodium hydroxynaphthoate (NaHN)). They attributed this persistent birefringence to the $\pi - \pi$ interactions present in the HNC aromatic salt. Further, Mishra *et al.*^{19,20} studied an aqueous mixture of the cationic surfactant [CTAB]=60 mM and [SHNC]=100 mM and observed that a mild tilt or tap could induce pronounced birefringence lasting for milliseconds. We observed that the precursor showed flow birefringence before and after passing through the micropost array, indicating the formation of anisotropic structures, also known as shear induced structures (SIS)^{19,20,29,48,49} (see Fig. 3 (B&C)). When an isotropic entangled micellar network is sheared, segments of the wormlike micelles can disentangle and align with the flow direction to exhibit birefringence^{29,48}. We used an EXICOR^R MICROIMAGERTM (Hinds Instruments, Inc.) which allowed us to observe the orientation of micelles when they passed through the micropost arrays. Figures 4 (A&B) show the birefringence behavior of the precursor before (A) and after passing (B) the micropost array. The blue color of these images is due to the background (PDMS-glass) subtraction by using a LED light source with a wavelength of 530 nm. The bright bands indicate the flow-alignment of the micelles, where in this case wormlike micelles are being aligned almost parallel to $x - axis$ based on our frame of reference (red $x - y$ coordinates). Figure 4 (C) presents a snap shot of FISP-like fingers flowing downstream in the microchannel under standard illumination. Figure 4 (D) exhibits the birefringence behavior of the FISP-like fingers under flow. The interface of the precursor-FISP shows birefringence response (bright areas), suggesting that at the interface the FISP structure is being aligned in the flow direction. However, the interior of the FISP-like fingers do not exhibit birefringence due to heterogenous structure of the FISP.

3.2 Rheology of the precursor and FISP

Fig. 5 shows the shear viscosity of the precursor as a function of the shear rate. The precursor solution showed a shear thinning response once a critical shear rate was reached ($\dot{\gamma}_c \sim 0.85 \text{ s}^{-1}$). The inset in Fig. 5 suggests the presence of shear banding in the precursor, based on the shear stress versus shear rate curve (highlighted flat region in the curve τ vs $\dot{\gamma}$). Shear banding behavior has been related to the presence of aligned wormlike micellar structures with flow birefringence

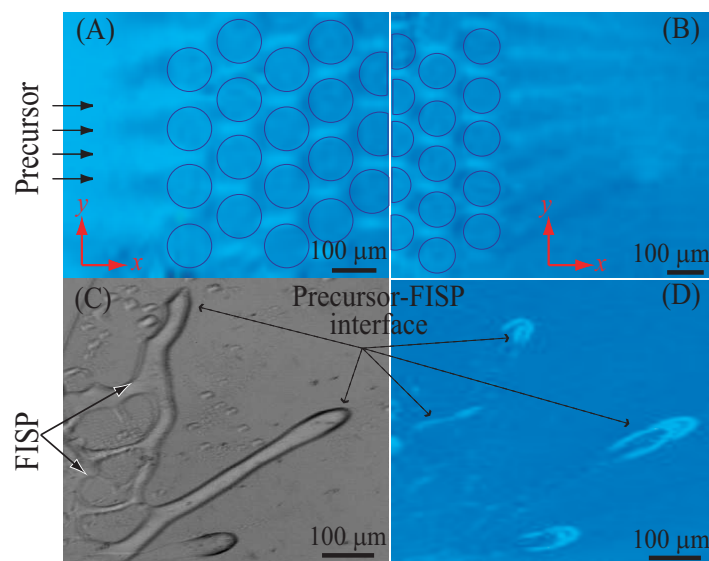


Fig. 4 (A&B) Flow birefringence of the precursor before and after passing the micropost array. The bright bands show the flow alignment of the micelles along the direction of the flow ($x - axis$). (C) FISP-like fingers flowing downstream in the microchannel. (D) Birefringence response at the FISP-precursor interface. The experiments were performed at 25 °C.

response^{29,49}. Small amplitude oscillatory shear measurements were conducted in the linear viscoelastic regime. The viscoelasticity behavior in the precursor can be correlated with single-mode Maxwellian relationship. This stress relaxation time λ_{eff} can be extracted from the first cross-over between the viscous modulus (G'') and the elastic modulus (G'). When the kinetic process of micellar breaking and reforming dominates, the fluid shows the Maxwellian behavior with a single exponential decay in the stress function with a single relaxation time^{50,51}. However, when the micellar breakup time is long compared with reptation time, dynamic properties of these micellar solutions are dominated by reptation processes^{51,52}. In the reptation process, stress relaxation is induced by the gradual disentanglements of micellar chains along the curvilinear tube environment, resulting in a deviation from single Maxwell mode. The range of frequencies was varied from 0.01 to 100 Hz. Fig. 6 shows good agreement between the bulk rheometry and the 2PPM of precursor within the ω limit from the bulk rheometry (blue symbols and black solid curve).

2PPM was performed due to the highly inhomogeneous structure of the FISP (see Fig. 12). We determined the correlated displacements of particles separated by a distance, $5 \mu\text{m} < r < 100 \mu\text{m}$. Fig. 6 also shows the frequency dependent behavior ($G'(\omega)$ and $G''(\omega)$) of the FISP approximated by two point microrheology. Importantly, 2PPM does not require the experimental data to be fit to analytical mod-

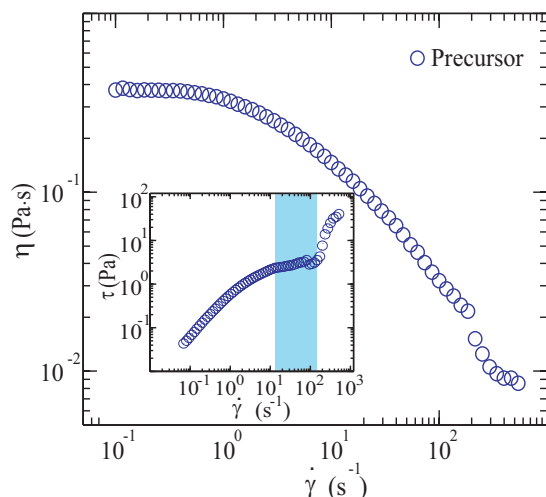


Fig. 5 Shear viscosity versus shear rate for precursor solution exhibiting shear thinning behavior above a critical shear rate ($\dot{\gamma} \sim 0.855 \text{ s}^{-1}$). The inset shows the non-monotonic behavior of the stress versus shear rate, suggesting the presence of shear banding (shaded blue area). The measurements were conducted at $25 \text{ }^\circ\text{C}$.

els due to the power law approximation of the mean-square displacement^{32,35}. From the crossover between $G'(\omega)$ and $G''(\omega)$ we approximated the value of the relaxation time (λ_{eff}) of both precursor and FISP. The plateau elastic modulus G_0 is the value at which G' showed a constant plateau at high frequencies, and the zero shear viscosity (η_0 was either measured from the bulk rheometry for the precursor, or calculated based on $\eta_0 = G_0 \lambda_{\text{eff}}$ for the FISP⁵³). G_0 of the precursor was obtained by relating the λ_{eff} from microrheology or bulk rheometry and the η_0 from bulk rheometry, yielding $G_0 = \eta_0 / \lambda_{\text{eff}}$ ⁵³. Table 1 summarizes the rheological properties of both precursor and FISP. The zero shear viscosity η_0 and the elastic modulus G_0 of the FISP are one order of magnitude larger than those of the original precursor. Interestingly, the relaxation time λ_{eff} of the precursor and FISP was not strongly affected, maintaining the same order of magnitude after the structural transition from precursor to FISP.

Table 1 The longest relaxation time λ_{eff} , plateau modulus G_0 , and the zero-shear viscosity η_0 for the precursor and FISP

Materials	η_0 (Pa·s)	λ_{eff} (s)	G_0 (Pa)
precursor	0.41 ± 0.02	0.11 ± 0.01	3.6 ± 0.18
FISP	4.6 ± 0.26	0.42 ± 0.08	11 ± 3.3

Note that microrheology techniques could underestimate the rheological properties of viscoelastic fluids due to dynamic and static errors during the particle tracking⁵⁴, compressibility effects⁵⁵, and most importantly, the value of maximum separation distance (r) within the tracer particles to obtain their

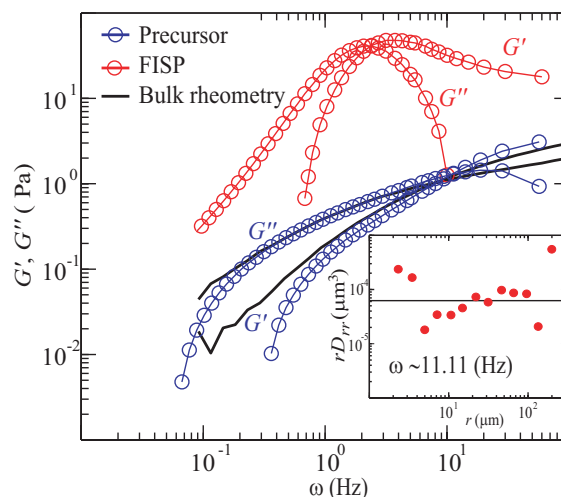


Fig. 6 Viscoelastic response of the precursor and FISP. The bulk rheometry (black solid line) and the two point microrheometry (blue circles) exhibit similar linear viscoelastic response. Red circles show the viscoelastic behavior of the FISP obtained by two point microrheometry. The inset shows the r dependence of rD_{rr} for $\omega \sim 11.11 \text{ Hz}$. The measurements were performed at $\sim 23 \pm 1.5 \text{ }^\circ\text{C}$.

cross-correlation motions⁵⁶. For instance, Fu *et al.*⁵⁵ reported that microrheology techniques could under-estimate the elastic modulus in polymer networks. They studied the effects of slip condition and compression effects on the tracer particle used in the microrheology. When slip conditions and compression effects are present at the same time, the elastic modulus in the polymer networks can decrease $\sim 43\%$ from the true value. Further, they observed that at low frequencies ($< 1 \text{ rad/s}$), the discrepancy between the bulk rheology and microrheology could be caused by the sliding and compression effects. In 2PPM the motion of the tracer particles induces the propagation of waves which are generated at the particle–fluid interface, which can reflect back and forth within the tracer particles^{32,56}. Hence, the cross-correlations of two tracer particles is dependent on the nature of these waves. Levine and Lubensky⁵⁷ showed that the cross-correlation function proposed by Crocker *et al.*³² was valid when the distance (r) between two tracer particles was larger than the radius of the particle. If the separation distance between two particles is large enough, the reflected waves decay significantly before reaching other tracer particles. However, if the separation distance is sufficiently short, reflected waves would have important contributions on the motion of particle tracers⁵⁶. Hence, the viscoelastic response of the material is affected by the separation distance of the tracer particles. All these factors (video-tracking of tracer particles, compressibility effects and the correct definition of separation distance within tracer particles) can affect the microrheology measurements of the FISP.

Nevertheless, this study provides a reasonable estimate of the rheological properties of the FISP.

3.3 Neutron Scattering of the Precursor and FISP

We first performed SANS and USANS in both precursor and FISP at room temperature 25 °C. We observed a clear structural transition from the precursor to the FISP (see Fig. 7). At high- q we fitted both precursor and FISP spectra to a flexible cylinder model³⁹. The fitting of the FISP provided a cylinder radius and length of ~ 2.3 nm and ~ 24 nm respectively. Whereas the fitting of the precursor gave a cylinder radius and length of ~ 2.3 nm and ~ 22 nm respectively. At high- q the cross sectional area of the wormlike micelles of both FISP and precursor remains constant. However, the length of the micelles in FISP is larger than that of the precursor, indicating that wormlike micelles grow slightly after passing through the micropost array.

At low- q , the SANS spectra of the FISP (red squares in Fig. 7) differs significantly from that of the precursor (blue circles in Fig. 7), exhibiting a gel-like scattering pattern with large domains⁵⁸. At $q < 0.03 \text{ \AA}^{-1}$ the spectrum of the precursor showed a plateau, indicating the absence of larger structures in the precursor. Meanwhile the spectrum of the FISP begins to increase with decreasing q , implying the presence of larger structures. We fitted the low- q spectra of the FISP to a fractal model based on the Teixeira model to evaluate the network scale structure of the FISP^{39,58}, which is primarily reflected in the USANS spectra ($q < 10^{-3} \text{ \AA}^{-1}$). From the fitting, we obtained a fractal dimension (D_f) of 2.95 ± 0.05 and correlation length (C_l) of $\sim 500 \pm 136$ nm. The value of D_f is representative of gel-like networks with characteristic size (C_l) on the order of several nanometers³⁹. Our TEM images (see inset in Fig. 7 and Fig. 12) display the formation of the size of micellar networks of ~ 200 – 700 nm. However the SANS data is not adequate to prove unequivocally that the FISP is composed by wormlike micellar bundle networks because of the lack of a structure factor suitable to describe the FISP. Therefore it is critical to combine complementary structural interrogation techniques (SEM, TEM, microrheology, and SANS) presented in this work to deduce that the FISP is formed by highly entangled and multi-connected micellar networks.

Next we investigated the temperature effects on the structure of both the precursor and FISP by varying temperatures at 25 °C, 30 °C, 45 °C, and 60 °C. We fit the precursor spectra by using a flexible cylinder model to obtain the Kuhn length (l_k), contour length (L), and radius of the micelle^{39,59}. The persistence length (l_p) can be related through $l_k = 2l_p$ ^{1,59}. Based on the fitting parameters, the precursor structure consists of semi-flexible cylindrical micelles with a radius of ~ 2.3 nm that is independent of the temperature range of this study. The contour length L of the cylinder decreased monotonically

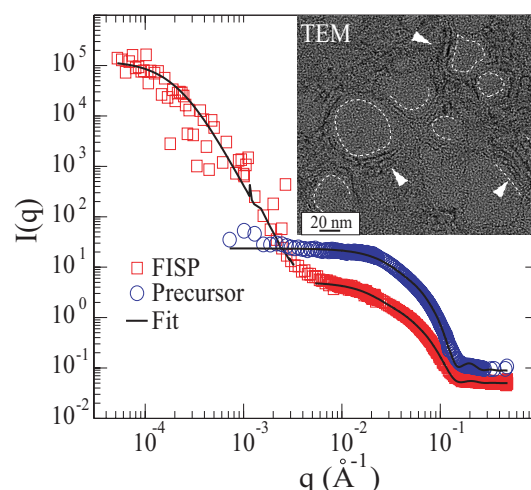


Fig. 7 Combined SANS and desmeared USANS spectra of the FISP (red squares), compared with the precursor SANS scattering (blue circles). The low- q spectrum was fitted to a fractal model (solid black line). The fit yields a fractal dimension of $D_f = 2.95 \pm 0.05$ and correlation length $C_l = 500 \pm 136$ nm. D_f suggests the formation of network structure. The inset is a TEM image of the FISP showing network-like structures. The high- q spectra of both FISP and precursor were fitted to a flexible cylinder model (black solid line). The fit of the FISP shows a cylinder diameter of ~ 2.3 nm with length of ~ 25 nm. Whereas, the fit of the precursor shows a cylinder diameter of ~ 2.3 nm with length of ~ 22 nm.

as the temperature increased, with $L \sim 22$ nm at 25 °C, $L \sim 21$ nm at 30 °C, $L \sim 20$ nm at 45 °C, and $L \sim 16$ nm at 60 °C (see Fig. 8). However, the persistence length $l_p \sim 4.5$ nm remained fairly constant for all the temperatures studied, suggesting that the flexibility of the micelles does not change by increasing temperatures (see Fig. 8). Hence we can approximate the flexural rigidity κ of the micelles using relationship $l_p = \kappa/k_B T$, yielding $\kappa = 4.5 k_B T \cdot \text{nm}$ ^{39,59}. Kalur *et al.*²¹ reported the SANS spectra of EHAC/SHNC (high concentration of [SHNC] = 360 mM) wormlike micellar solutions as the temperature increased from 25 °C to 65 °C. They found that the cross-sectional radius of the micelles remained constant (~ 2.6 nm) with the temperature variation. However, structural transition from spherical micelles (~ 2.6 nm in radius) to cylindrical micelles (~ 2.6 nm in radius and length ~ 60 nm) was observed with increasing temperatures. Although the micellar structural transition reported by Kalur *et al.* shows the opposite trend as that reported in this work, the micellar dimensions of the precursor are on the same order of magnitude as those presented by Kalur *et al.*²¹. The inset in Fig. 8A plots the zero shear viscosity of the precursor with respect to different temperatures. The zero shear viscosity η_0 of the precursor decreases as the temperature increases, correlated with the shortening of the contour length L (from ~ 25 nm at 25 °C

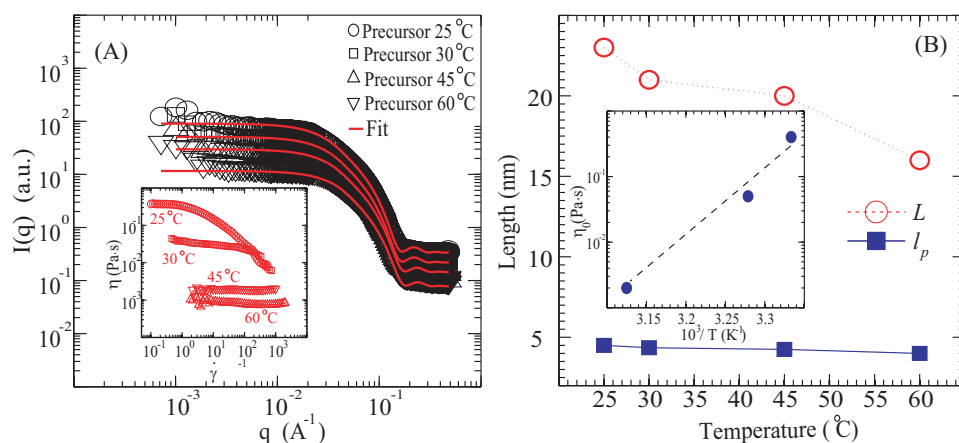


Fig. 8 (A) SANS spectra of the precursor at different temperatures. A flexible cylinder model was used to fit the spectra of the precursor. The inset in (A) presents the zero shear viscosity of the precursor at different temperatures. (B) Variation of the contour length (L) and persistence length (l_p) of the cylindrical micelles at increasing temperatures. The inset in (B) shows an Arrhenius plot of the zero-shear viscosity η_0 against $1/T$. The slope of the dash line yields the activation energy ($E_a \sim 36 k_B T$) of the precursor.

to ~ 16 nm at 60°C) in the precursor solution.

We also measured the plateau modulus G_0 of the 45 mM SHNC/CTAB precursor solution at temperatures 25°C , 30°C , 45°C , and 60°C under small-amplitude oscillatory shear (see supporting information). For temperatures from 25°C – 45°C , the plateau modulus of the precursor solution remains a constant ($G_0 \sim 3.6$ Pa), while the precursor solution exhibits Newtonian-alike behavior at 60°C . Similarly, Raghavan *et al.* observed that G_0 of cationic surfactants with long (C_{22}) mono-unsaturated tails was independent of temperature variations at frequencies larger than 100 Hz⁶⁰. Based on the above information, we fit the measured zero shear viscosity of 45 mM SHNC/CTAB precursor solution with the Arrhenius relationship ($\eta_0 = AG_0 e^{E_a/RT}$) to approximate the flow activation energy (E_a) of the precursor solution with temperatures ranging from 25°C to 45°C , while fixing the value of $G_0 \sim 3.6$ Pa. The inset in Figure 8 (B) shows the Arrhenius plot (η_0 against $1/T$) of the precursor solution, where the slope of the dash line yields the value of $E_a \sim 36 k_B T$ ^{60–64}. This value of E_a falls in the range of values found for other CTA based micellar solutions ($E_a \sim 20$ – $80 k_B T$)^{60–62}.

Fig. 9 presents the high- q SANS spectra of the FISP at higher temperatures. We observed a monotonic decrease in the SANS spectra of the FISP by increasing temperature at $q > 10^{-2} \text{\AA}^{-1}$, implying the structural transition in the FISP at the sub-nanometer scale. In particular, a drastic structural transition from 45°C to 60°C was observed in the FISP spectra at $q > 10^{-2} \text{\AA}^{-1}$. The FISP's spectra can be fit to a cylinder model for the temperatures 25°C , 30°C , and 45°C , while the FISP's spectra at 60°C can be fit to a spherical model with a radius of ~ 3 nm. From the cylindrical fitting, the radius of the cylinder remained constant (~ 2.4 nm) for all three tem-

peratures (25°C , 30°C , 45°C) examined, while the length of the cylinder (L) becomes shorter with increasing temperatures, with ~ 25 nm at 25°C , ~ 19 nm at 30°C , and ~ 17 nm at 45°C .

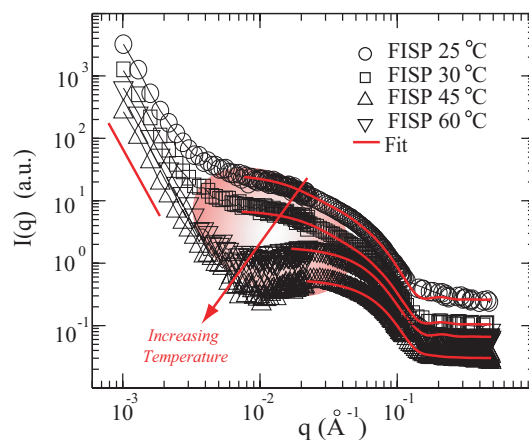


Fig. 9 SANS spectra of the FISP at different temperatures. At low- q the structure of the FISP is not affected with increasing temperatures. At low- q we used a power law fitting for the FISP structure and found an index power of $\sim 3.5 \pm 0.05$. At high- q and for the temperatures of 25°C , 30°C and 45°C , we fitted the FISP's spectra to a flexible cylinder model. The length (L) of the wormlike micelles become shorter by increasing temperatures: $L=25$ nm (25°C), $L=22$ nm (30°C), and $L=20$ nm (45°C). The radius remained constant at ~ 2.4 nm for the three temperatures. At 60°C and high- q , the best fit was obtained by using a sphere model. The radius obtained from the fit was ~ 3.0 nm.

Regarding the fitting model, we attempted to fit the spectra of the FISP at 60°C by using both an ellipsoid model and

elliptic-cylinder model. However, the sphere model gave the best least squared error in the fit. The increase of the FISP's spectra at low- q suggests the potential presence of large structures in the FISP. At $q < 10^{-2} \text{ \AA}^{-1}$, the FISP's spectra exhibited the same trend for all the temperatures studied, implying that the large structure of the FISP remains intact with increasing temperatures. We fitted the spectra at low- q for all the temperatures studied to a power law model and found a power index of $\sim 3.5 \pm 0.05$. The slope indicates the homogeneity of the body-media interface (i.e., FISP-deuterium interface). We speculate that the high entanglement density ($\nu = \frac{G_0}{k_B T} \approx 27.5 \pm 1.5 \times 10^{21} \text{ m}^{-3}$)⁵³ of the FISP is critical to maintain the FISP's structure at high temperatures. The naphthalene structure in the SHNC can induce higher aromatic interactions ($\pi - \pi$ and cation- π) within micelles, hence increasing attractive potential in wormlike micelles^{48,65,66}. Further, Hassan *et al.*^{14,67} reported that strong hydrophobicity (e.g., SHNC) induces high stability of micelles at high temperatures. Such noncovalent interactions in the FISP can be sufficient to counteract the tendency of wormlike micelles to dissociate at high temperatures, preserving the FISP structure.

3.4 Localized temperature behavior of the FISP

Gold etched microheaters were fabricated to study the local behavior of the FISP at different temperatures (see Fig. 2). First, we formed the FISP at room temperature with the micropost device. Once sufficient amount of FISP was generated and collected to the area of the microheater, we rinsed the microchannel with DI-water to remove the left over precursor before increasing the temperature from 25 °C to 60 °C (see Fig. 2B). We recorded videos of the FISP at higher temperatures by using a magnification of 100×/1.30 oil objective with a 1.5× tube lens.

Qualitatively, we did not observe any disintegration in the FISP structure from 25 °C to ~ 45 °C. However, when the temperature was increased to 47 ± 1.5 °C, droplets emerged inside the FISP structure (see Fig. 10 and Fig. 11 and video in the supporting information). We suspect that the weakest bonds in both wormlike micelles and the micellar bundle network of the FISP start to disintegrate at $\sim 47 \pm 1.5$ °C, inducing droplet formation. The rupture of the weakest bonds in the FISP structure first led to the increase of the pore size in FISP, which allowed some DI-water to penetrate the FISP structure, yielding the formation of droplets. We infer that the droplets are composed by a mixture of precursor and water (see Fig. 3D 10). Fig. 11 shows snapshots of the structural evolution of the FISP at $\sim 47 \pm 1.5$ °C. The white stars in Fig. 11 highlight some precursor droplets formed in the FISP structure. We observed the formation-disintegration of precursor-water droplets inside the FISP structure in a cyclic fashion for long periods of time (> 10 hours). Further, the cyclic formation-disintegration of

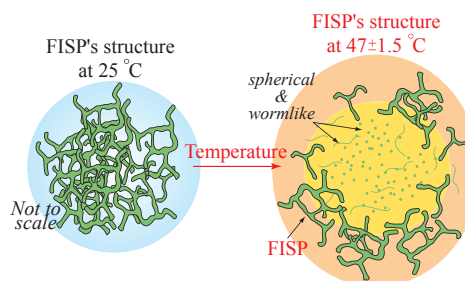


Fig. 10 Schematics representation of the FISP's structure by increasing temperature. At room temperature the FISP exhibits highly entangled and multi-connected micellar network. At temperatures above $\sim 47 \pm 1.5$ °C, the weakest micellar bonds in the FISP begin to disintegrate, enhancing the formation of droplets containing the mixture of precursor and water (yellow region in the schematics). Further, the increase of temperature also induces the formation of larger pores in the FISP structure, as well as the breaking and shortening of micellar bundles and wormlike micelles.

precursor-water droplets inside the FISP was also observed at ~ 60 °C without showing complete disintegration of the FISP (see compiled video in the supporting information), which is consistent with the SANS data. At $q < 5 \times 10^{-3} \text{ \AA}^{-1}$, the FISP's spectra showed no disintegration of FISP at high temperatures. The formation of precursor-water droplets observed in the microheater might be related to the structural transition observed from the SANS spectra of the FISP at high temperature in the high- q regime.

3.5 Microstructure of the FISP

Based on SEM and TEM images (see Fig. 12), the thickness and length of micellar bundles range between ~ 10 – 300 nm and ~ 80 – 400 nm respectively, indicating that a single micellar bundle consists of several individual wormlike micelles. Based on the TEM images, the diameter of the wormlike micelles in the FISP has a value of $\sim 4 \pm 0.9$ nm, consistent with that from the SANS measurements (~ 4.8 nm). The existence of ionic micellar bundles was possibly related to the electrostatic interactions from the counter-ions present in the ionic surfactant solution^{68,69}. Barentin and Liu⁶⁹ proposed that electrostatic attractions could lead to the formation of micellar bundles from an ionic surfactant solution. They showed that the energy required to form micellar bundles was linearly dependent on the thickness of the bundle and that the micellar bundles might be a metastable phase in the micellar solution.

We observed two distinct structural domains in the FISP structure. Fig. 12 (top row) exhibits highly entangled and multiconnected micellar bundles, similar to the structure observed by Cardiel *et al.*²³ for NaSal/CTAB based FISP. However, we noticed a more ordered structure with well defined circular pores in the SHNC/CTAB based FISP (see Fig. 12 bottom

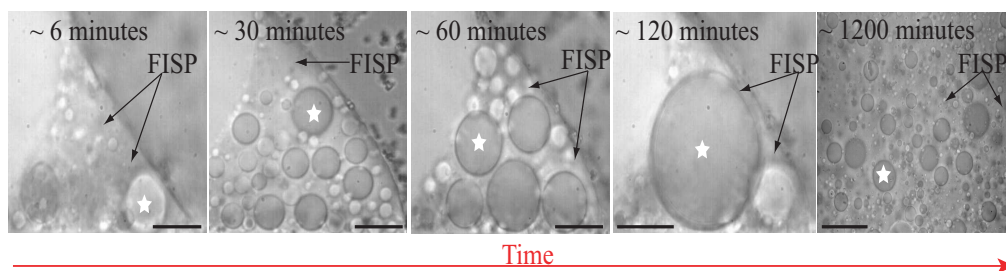


Fig. 11 Inside of the FISP structure the formation of precursor droplets begins to occur at $\sim 47 \pm 1.5$ °C. The most notorious precursor droplets are formed after ~ 6 minutes. A cycle of formation and breaking up of precursor-water droplets is observed for long periods of time. No complete disintegration of the FISP was observed even after ~ 1200 minutes. See more details in the supporting information movie. Scale bar is $20\mu\text{m}$.

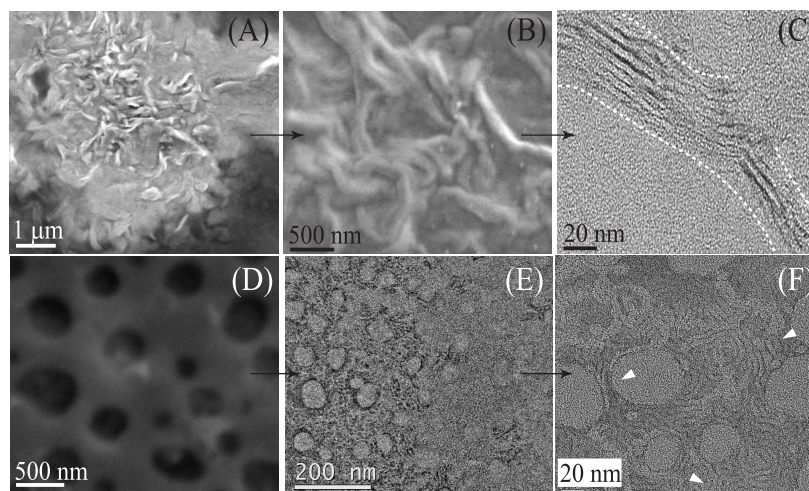


Fig. 12 (A&B) SEM images of the FISP showing highly entangled micellar bundle-like structures. (C) TEM image of one of the bundles observed in (B). The bundle is formed by individual wormlike micelles with diameter ~ 5 nm. (D) SEM image of the FISP exhibiting mesh-like micellar structures with pore wide range of pore size (~ 50 – 800 nm). (E&F) TEM images of one of the regions observed in (D), (E&F) presents the formation of bundle-like micellar loops. The diameter of the loops ranges on 10 – 50 nm with a bundle-like diameter of ~ 20 nm.

row). Fig. 12 (D) is an SEM image showing a region with the well ordered FISP structure. Fig. 12(E&F) are TEM images showing well defined circular pores (micellar loops) in the FISP. The micellar loops range from 10 nm to 50 nm in diameter.

We approximated the loop size of the FISP by using the mesh size concept (ξ) in wormlike micellar structures. Shikata *et al.*^{45,70,71} proposed that the elasticity of an aqueous CTAB based wormlike micellar solution was originated from the excessive entropy caused by the orientation of some micellar chains between entangled points. This mechanism is similar to those observed in the concentrated rubber systems⁵³. Assuming a Gaussian distribution of the wormlike micelles, rubber elasticity relates the elastic modulus and the thermal energy to the hydrodynamic correlation length (or the network mesh size ξ) as follows:

$$\xi^3 = \frac{k_B T}{G_0} \quad (8)$$

G_0 can be obtained from the microrheology data of the FISP. The estimated mesh size from equation 8 ($\xi \approx 70$ nm) and the mesh size obtained from TEM images ($\xi^* \approx 10$ – 50 nm) has the same order of magnitude, despite the error introduced from the TEM sample preparation, artifacts and system errors.

Horbaschek *et al.*¹⁵ and Abdel-Rahem *et al.*⁶ studied microstructures for equal molar 100 mM CTAB and SHNC system. They observed densely packed vesicles and multilamellar vesicles of 100 – 800 nm in diameter and 60 nm in thickness under FF-TEM electron micrographs, where some of the vesicles showing diameter of $\sim 20\mu\text{m}$. They proposed that since SHNC behaved similar to anionic surfactant but with a shorter tail, the SHNC/CTAB mixture at equal molar

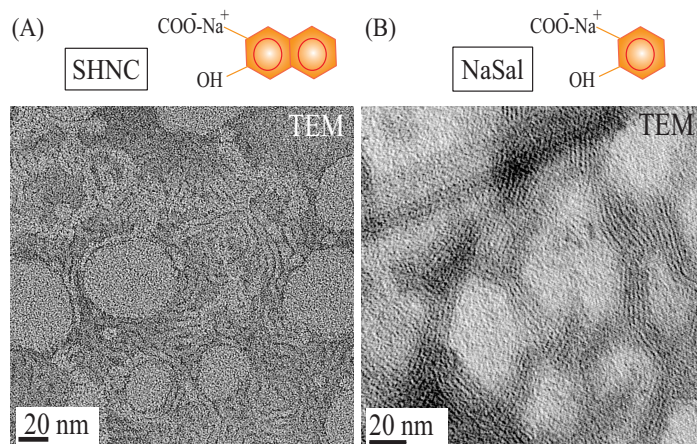


Fig. 13 (A) Chemical structure of SHNC and TEM image of the FISP_{SHNC}. (B) Chemical structure of NaSal and TEM image of the FISP_{NaSal}.

concentration was able to form bilayers and vesicles⁷². In addition, the excess salt ions (Na⁺ from SHNC) shield the charge of the bilayers and screen the charges between vesicles. As a result, smaller vesicles collapse and form thick precipitates with larger dimensions. We are not necessarily claiming the vesicle formation in the FISP, but similar argument can apply: under flow, the closely packed microposts induce concentration fluctuations in the precursor, where HNC⁻ penetrated CTAB micelles and π - π and cation- π interactions come to play between adjacent micelles. As a result, formation of circular porous bilayer structures can be induced. Due to the screening effects of the free salt ions charged between bilayers, smaller pores collapse with each other and lead to a wide size distributions.

3.6 Comparison between SHNC/CTAB based FISP and NaSal/CTAB based FISP

Recently we have reported the formation of FISP by using the organic salt NaSal²³. In this section, we briefly compare the structure of the FISP made of NaSal/CTAB (FISP_{NaSal}) and the FISP made of SHNC/CTAB (FISP_{SHNC}). With very similar CTAB concentrations (50 mM in NaSal/CTAB system²³ and 45 mM in CTAB/SHNC system) and the same salt/surfactant ratio ($R = 0.32$), we were able to produce flow induced structure phases (FISP_{NaSal} and FISP_{SHNC}) from both precursor solutions (NaSal/CTAB and SHNC/CTAB) by using microfluidics. Compared with NaSal, SHNC is a much stronger hydrotropic salt with double benzene rings (see Figure 13), in which case, the surface activity of CTAB micelles is greatly reduced from decreased spontaneous curvature of micelles.

Figure 13 shows the chemical structure and its corresponding TEM image for both FISP_{SHNC} and FISP_{NaSal} structures.

Broadly speaking, both FISPs exhibit similar micellar bundle-like networks with mesh size ranging from 20 nm to a few microns (see Figure 13). TEM imaging procedure can induce sample preparation artifacts (e.g., drying effects), which can potentially alter the true structure of the sample. Hence, we compared the combined USANS-SANS scattering of both FISPs for the hydrated structures of the FISPs (see Figure 14). We fit the spectra of both FISPs to a fractal model (low- q range) and flexible cylinder model (high- q range)^{39,58}. From the fractal model we obtained similar fractal dimensions of $\sim 2.95 \pm 0.05$ and $\sim 2.9 \pm 0.006$ for FISP_{SHNC} and FISP_{NaSal} respectively. The fractal dimension of both FISPs indicates that the FISPs is composed by fibrillar networks^{39,58}. Further, the fractal model also provides an approximation of the domain size (correlation length C_l) present in the FISPs at low- q . We obtained a correlation length of $C_{l,SHNC} = 0.5 \pm 0.136 \mu\text{m}$ for the FISP_{SHNC} and $C_{l,NaSal} = 3.4 \pm 0.4 \mu\text{m}$ for the FISP_{NaSal}. From the flexible cylinder model, we obtained the Kuhn length (l_k), contour length (L) and radius (r) of the micelles at high- q . We then approximated the persistence length (a measure of the flexural rigidity of the micelles) by using $l_k = 2l_p$ ^{29,30,59}. The fitting of the high- q spectra of the FISP_{SHNC} provides values of $l_k = 9 \text{ nm}$, $L = 25 \text{ nm}$, $r = 2.3 \text{ nm}$, and $l_p = 4.5 \text{ nm}$. Whereas the fitting of the scattering of FISP_{NaSal} yields values of $l_k = 3.6 \text{ nm}$, $L = 21 \text{ nm}$, $r = 2.2 \text{ nm}$, and $l_p = 1.3 \text{ nm}$. Both FISPs' spectra present similar structural dimensions (C_l , D_l , l_k , L , r , and l_p). Nevertheless, the scattering data suggested that the FISP_{NaSal} is a more flexible structure with larger domains (correlation length $C_{l,NaSal} \sim 3.4 \pm 0.4 \mu\text{m}$) in comparison to that of FISP_{SHNC}.

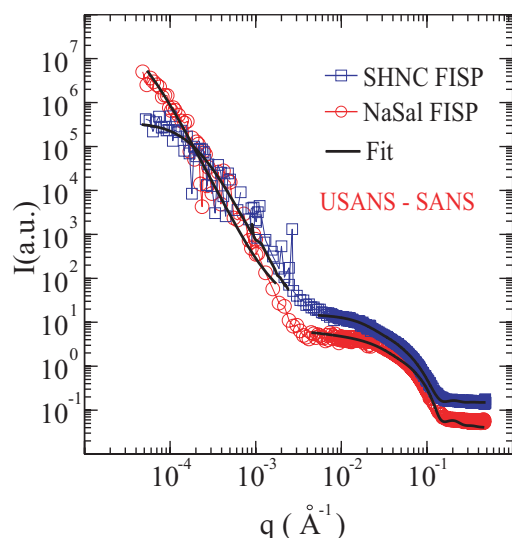


Fig. 14 Combined SANS and desmeared USANS spectra of both FISPs. The spectra of the FISPs were fitted to a fractal model (low- q region) and flexible cylinder model (high- q region). The fit of FISP_{SHNC} yields a fractal dimension of $D_{f,SHNC}=2.95\pm 0.05$ and correlation length $C_{l,SHNC}=0.5\pm 0.136\ \mu\text{m}$. D_f . While the fit of FISP_{NaSal} yields $D_{f,NaSal}=2.9\pm 0.006$ and correlation length $C_{l,NaSal}=3.4\pm 4\ \mu\text{m}$. From the flexible cylinder model, the scattering of the FISP_{SHNC} yields a Kuhn length (l_k) of ~ 9 nm, contour length (L) of ~ 25 nm, radius (r) of ~ 2.3 nm, and persistence length (l_p) of ~ 4.5 nm. While the scattering of FISP_{NaSal} yields values of $l_k \sim 3.6$ nm, $L \sim 21$ nm, $r \sim 2.2$ nm, and $l_p \sim 1.8$ nm.

4 Conclusions

In summary, we observed the formation of a stable micellar network (FISP) by using a mixture of $\pi - \pi$ hydrotropic organic salt (SHNC) and cationic surfactant CTAB in the semi-dilute regime by using a microfluidic device containing micropost arrays, by simply tuning the flow condition and microspatial confinement under room temperature. We proposed that the formation of FISP followed the same mechanism that was suggested by Cardiel *et al.*²³, where spatial confinement from the micropost array, entropic and local micellar fluctuations in the micropost array induced the formation of branched micellar networks. The SHNC/CTAB precursor solution exhibited flow birefringence, while such response disappeared in the FISP, possibly due to the thickness and high entanglement density in the FISP. We also showed that a weakly viscoelastic micellar precursor could transition to a more viscoelastic micellar network structure. The zero shear viscosity of the precursor is around one order of magnitude smaller than that of its FISP. We also observed that the FISP did not disintegrate at relatively high temperatures (30, 45, and 60 °C) by using SANS and direct microscopy visualization from a microheater setup. However, precursor droplets began to form

in the FISP at temperature ≥ 47 °C. Nevertheless, we did not observe a complete disintegration of the FISP at high temperatures.

5 Acknowledgement

We gratefully acknowledge support from the National Science Foundation CBET-1335666 and the OIST Graduate University with subsidy funding from the Cabinet Office, Government of Japan (AQS, JJC). This work benefited from SasView software, originally developed by the DANSE project under NSF DMR-0520547. This work utilized facilities supported in part by the National Science Foundation under Agreement No. DMR-0944772. We acknowledge the support of the National Institute of Standards and Technology, U.S. Department of Commerce, in providing the neutron research facilities used in this work. JJC is thankful for a CONACYT-PhD fellowship.

References

- 1 J. N. Israelachvili, *Intermolecular and Surface Forces: With Applications to Colloidal and Biological Systems*, Academic Press, London, 1985.
- 2 J. C. Brackman and J. Engberts, *Langmuir*, 1991, **7**, 2097–2102.
- 3 V. Hartmann and R. Cressely, *Colloids Surf., A*, 1997, **121**, 151–62.
- 4 W. J. Kim and S. M. Yang, *J. Colloid Interface Sci.*, 2000, **232**, 225–234.
- 5 C. Oelschlaeger, G. Waton and S. J. Candau, *Langmuir*, 2003, **19**, 10495–500.
- 6 R. Abdel-Rahem, *Adv. Colloid Interface Sci.*, 2008, **141**, 24–36.
- 7 T. Shikata, H. Hirata and T. Kotaka, *Langmuir*, 1987, **3**, 1081–1086.
- 8 E. Mendes, J. Narayanan, R. Oda, F. Kern, S. J. Candau and C. Manohar, *J. Phys. Chem. B*, 1997, **101**, 2256–2258.
- 9 U. R. K. Rao, C. Manohar, B. S. Valulikal and R. M. Iyer, *J. Phys. Chem.*, 1987, **91**, 3286–3291.
- 10 Y. Y. Lin, Y. Qiao, X. H. Cheng, Y. Yan, Z. B. Li and J. B. Huang, *J. Colloid Interface Sci.*, 2012, **369**, 238–244.
- 11 T. K. Hodgdon and E. W. Kaler, *Curr. Opin. Colloid Interface Sci.*, 2006, **12**, 121–128.
- 12 M. H. Hatzopoulos, J. Eastoe, P. J. Dowding, S. E. Rogers, R. Heenan and R. Dyer, *Langmuir*, 2011, **27**, 12346–12353.
- 13 D. Subramanian, C. T. Boughter, J. B. Klauda, B. Hammouda and M. A. Anisimov, *Faraday Discuss.*, 2013, 217–238.
- 14 P. A. Hassan, J. Narayanan, S. V. G. Menon, R. A. Salkar, S. D. Samant and C. Manohar, *Colloids Surf., A*, 1996, **117**, 89–94.
- 15 K. Horbaschek, H. Hoffmann and C. Thunig, *J. Colloid Interface Sci.*, 1998, **206**, 439–456.
- 16 R. Abdel-Rahem, M. Gradzielski and H. Hoffmann, *J. Colloid Interface Sci.*, 2005, **288**, 570–582.
- 17 S. Gravsholt, *J. Colloid Interface Sci.*, 1976, **57**, 575–577.
- 18 C. Oelschlaeger, P. Suwita and N. Willenbacher, *Langmuir*, 2010, **26**, 7045–7053.
- 19 B. K. Mishra, S. D. Samant, P. Pradhan, S. B. Mishra and C. Manohar, *Langmuir*, 1993, **9**, 894–898.
- 20 S. Mishra, B. K. Mishra, S. D. Samant, J. Narayanan and C. Manohar, *Langmuir*, 1993, **9**, 2804–2807.
- 21 G. C. Kalur, B. D. Frounfelker, B. H. Cipriano, A. I. Norman and S. R. Raghavan, *Langmuir*, 2005, **21**, 10998–11004.
- 22 G. Verma, V. K. Aswal, G. Fritz-Popovski, C. P. Shah, M. Kumar and P. A. Hassan, *J. Colloid Interface Sci.*, 2011, **359**, 163–170.

- 23 J. J. Cardiel, A. C. Dohnalkova, N. Dubash, Y. Zhao, P. Cheung and A. Q. Shen, *Proc. Natl. Acad. Sci. U. S. A.*, 2013, **110**, E1653–E1660.
- 24 P. Cheung, N. Dubash and A. Q. Shen, *Soft Matter*, 2012, **8**, 2304–2309.
- 25 I. A. Kadoma and J. W. van Egmond, *Phys. Rev. Lett.*, 1996, **76**, 4432–4435.
- 26 E. Helfand and G. H. Fredrickson, *Phys. Rev. Lett.*, 1989, **62**, 2468–2471.
- 27 T. Podgorski, M. C. Sostarecz, S. Zorman and A. Belmonte, *Phys. Rev. Lett.*, 2007, **76**, 016202.
- 28 S. Lerouge, M. Argentina and J. P. Decruppe, *Phys. Rev. Lett.*, 2006, **96**, 08830.
- 29 J. F. Berret, *Rheology of Wormlike Micelles: Equilibrium Properties and Shear Banding Transitions. in Molecular Gels*, Springer Netherlands, 2006.
- 30 C. A. Dreiss, *Soft Matter*, 2007, **3**, 956–70.
- 31 Y. Xia and G. M. Whitesides, *Angew. Chem. Int. Ed.*, 1998, **37**, 550–75.
- 32 J. C. Crocker, M. T. Valentine, E. R. Weeks, T. Gisler, P. D. Kaplan, A. G. Yodh and D. A. Weitz, *Phys. Rev. Lett.*, 2000, **85**, 888–891.
- 33 V. Pelletier, N. Gal, P. Fournier and M. L. Kilfoil, *Phys. Rev. Lett.*, 2009, **102**, 188303(1)–188303(4).
- 34 M. L. Gardel, M. T. Valentine, J. C. Crocker, A. R. Bausch and D. A. Weitz, *Phys. Rev. Lett.*, 2003, **91**, 158302(1)–158302(4).
- 35 T. G. Mason, *Rheol. Acta*, 2000, **39**, 371–378.
- 36 J. C. Crocker and D. G. Grier, *J. Colloid and Interface Sci.*, 1996, **179**, 298–310.
- 37 T. G. Mason, K. Ganesan, J. F. van Zanten, D. Wirtz and S. C. Kuo, *Phys. Rev. Lett.*, 1997, **79**, 3282–3285.
- 38 J. G. Barker, C. J. Glinka, J. J. Moyer, M. H. Kim, A. R. Drews and M. Agamalian, *J. Appl. Crystallogr.*, 2005, **38**, 1004–1011.
- 39 S. Kline, *J. Appl. Crystallogr.*, 2006, **39**, 895–900.
- 40 I. A. Kadoma, C. Ylitalo and J. W. van Egmond, *Rheol. Acta.*, 1997, **36**, 1–12.
- 41 I. A. Kadoma and J. W. van Egmond, *Langmuir*, 1997, **13**, 4551–4561.
- 42 T. J. Drye and M. E. Cates, *J. Chem. Phys.*, 1992, **96**, 1367–1376.
- 43 A. Khatory, F. Kern, F. Lequeux, J. Appell, G. Porte, N. Moire, A. Ott and W. Urbach, *Langmuir*, 1993, **9**, 933–939.
- 44 B. A. Schubert, E. W. Kaler and J. N. Wagner, *Langmuir*, 2003, **19**, 4079–4089.
- 45 T. Shikata, H. Hirata and T. Kotaka, *Langmuir*, 1988, **4**, 354–359.
- 46 S. Yamamoto and S. J. Hyodo, *J. Chem. Phys.*, 2005, **122**, 204907(1)–204907(8).
- 47 D. F. James and D. R. McLaren, *J. Fluid Mech.*, 1975, **70**, 733–752.
- 48 B. D. Frounfelker, G. C. Kalur, B. H. Cipriano, D. Danino and S. R. Raghavan, *Langmuir*, 2008, **25**, 167–172.
- 49 S. Lerouge and J. F. Berret, *Adv. Polym. Sci.*, 2009, **230**, 1–71.
- 50 M. E. Cates, *Macromolecules*, 1987, **20**, 2289–2096.
- 51 M. E. Cates and S. J. Candau, *J. Phys.: Condens. Matter*, 1990, **33**, 6869–6892.
- 52 T. J. Drye and M. E. Cates, *J. Chem. Phys.*, 1992, **96**, 1367–1375.
- 53 D. M. and E. S. F., *The Theory of Polymer Dynamics*, Oxford University Press, 1986.
- 54 T. Savin and P. S. Doyle, *Biophys. J.*, 2005, **88**, 623638.
- 55 H. Fu, V. Shenoy and T. Powers, *Phys. Rev. E*, 2008, **78**, 061503(1)–061503(14).
- 56 A. Crdoba, J. D. Schieber and T. Indei, *Phys. Fluids*, 2012, **24**, 073103(1)–073103(19).
- 57 A. Levine and T. Lubensky, *Phys. Rev. Lett.*, 2000, **85**, 1774–1777.
- 58 K. Weigandt, L. Porcar and D. Pozzo, *Soft Matter*, 2009, **5**, 4321–4330.
- 59 J. S. Pedersen and P. Schurtenberger, *Macromolecules*, 1987, **20**, 7602–7612.
- 60 S. R. Raghavan and E. W. Kaler, *Langmuir*, 2001, **17**, 300–306.
- 61 S. J. Candau, E. Hirsch, R. Zana and M. Delsanti, *Langmuir*, 1989, 1225–1229.
- 62 F. Kern, R. Zana and S. J. Candau, *Langmuir*, 1991, **7**, 1344–1351.
- 63 Y. Zhang, Y. Han, Z. Chu, S. He, J. Zhang and Y. Feng, *J. Colloid Interface Sci.*, 2013, **394**, 319328.
- 64 Y. Zhang, Y. Luo, Y. Wang, J. Zhang and Y. Feng, *Colloids Surf., A*, 2013, **436**, 71–79.
- 65 K. Bijma and J. B. F. N. Engberts, *Langmuir*, 1997, **13**, 4843–4849.
- 66 K. Bijma, E. Rank and J. B. F. N. Engberts, *J. Colloid Interface Sci.*, 1998, **205**, 245–256.
- 67 P. A. Hassan, B. S. Valaulikar, C. Manohar, F. Kern, L. Bourdieu and S. J. Candau, *Langmuir*, 1996, **12**, 4350–4357.
- 68 Z. Wang and R. Larson, *J. Phys. Chem. B*, 2009, **113**, 13697–13710.
- 69 C. Barentin and A. Liu, *Europhys. Lett.*, 2001, **55**, 432–438.
- 70 T. Shikata, H. Hirata, E. Takatori and K. Osaki, *J. Non-Newtonian Fluid Mech.*, 1988, **28**, 171–182.
- 71 T. Shikata, H. Hirata and T. Kotaka, *Langmuir*, 1988, **4**, 354–359.
- 72 E. W. Kaler, A. K. Murthy, B. E. Rodriguez and J. A. N. Zasadzinski, *Science*, 1989, **245**, 1371–1374.

